

RESEARCH ARTICLE

Engineering Reports

Open Access

WILEY

Study of mechanical properties and enhancing auxetic mechanism of composite auxetic structures

Zengqin Shi¹ | Qing Wang^{1,2}  | Yunfeng Li¹ | Ning Wang¹ | Lulu Lei¹ | Xiaodong Li¹

¹Institute of Nano Engineering, College of Civil Engineering and Architecture, Shandong University of Science and Technology, Qingdao, China

²College of Mechanical and Architectural Engineering, Taishan University, Tai'an, China

Correspondence

Qing Wang, Institute of Nano Engineering, College of Civil Engineering and Architecture, Shandong University of Science and Technology, Qingdao, 266590 Shandong, China.
Email: qwang@sdu.edu.cn

Funding information

Natural Science Foundation of Shandong Province, Grant/Award Number: ZR2017MA013; Taishan Scholar Project of Shandong Province, Grant/Award Number: TSHW20130956

Abstract

The auxetic structures attract much attention because of their good properties, such as enhanced energy absorption capacity and buckling resistance. It is an important topic to combine the auxetic structures with other materials or structures to improve their mechanical properties. In this paper, a composite auxetic structure was proposed, in which the embedded structure and re-entrant structure can deform independently to adjust the mechanical properties. Under uniaxial compression, the effects of changes in the embedded structure and re-entrant structure on Poisson's ratio, relative Young's modulus, and energy absorption of the composite auxetic structure were studied. By introducing the rate of change of mechanical properties, the effects of the embedded structure and re-entrant structure on the composite auxetic structure were studied. The results show that changing the embedded structure for Poisson's ratio and relative Young's modulus and changing the re-entrant structure for energy absorption can maximize the material utilization. And changing the re-entrant structure can make the mechanical properties of the composite auxetic structure reach a larger adjustable range. This study can provide a new way for the combination of future auxetic structures to meet the needs of different applications in civil engineering.

KEYWORDS

auxetic mechanism, embedded structure, flexible deformation, mechanical properties, re-entrant structure

1 | INTRODUCTION

Different from conventional materials, the auxetic structures (also termed metamaterials) have the unique property of negative Poisson's ratio. The auxetic structures contract (expand) laterally when they are vertically compressed (stretched). In 1987, Lakes¹ reported the first artificial auxetic structure in his experiment. Then researchers began to pay more and more attention to the auxetic structures. Many good properties were studied, such as enhanced buckling resistance,² shear modulus,³ indentation resistance,⁴ fracture toughness,^{5,6} and energy absorption capacity.⁷ These good properties are reported to be beneficial for many practical applications.^{8,9}

This is an open access article under the terms of the Creative Commons Attribution-NonCommercial License, which permits use, distribution and reproduction in any medium, provided the original work is properly cited and is not used for commercial purposes.

© 2021 The Authors. *Engineering Reports* published by John Wiley & Sons Ltd.

Up to now, many kinds of the auxetic structures have been developed, mainly including the re-entrant structures,¹⁰ rotating polygonal structures,¹¹ and chiral structures.¹² It is an important topic to combine the auxetic structures with other materials or structures to improve mechanical properties of the auxetic structures.^{13–15} In order to improve the stiffness of the auxetic structures, Fu et al.^{16,17} proposed two kinds of the composite auxetic structures that embed the x-structure and rhombic structure into the re-entrant structures, in which the effects of adjusting the angle of the proposed composite auxetic structures on Poisson's ratio and Young's modulus were studied. Chen et al.¹⁸ designed a combined enhanced honeycomb structure based on two existing embedded enhanced honeycombs. Li et al.¹⁹ investigated the yield strengths of the re-entrant structure and hexagonal structure with the embedded horizontal structure under the coupling effect of the shear and axial stress. They also found that the Young's modulus and strength of the auxetic structures can be designed independently with its Poisson's ratio by studying the re-entrant structure and double arrowhead structure with the embedded vertical structure.²⁰ When the auxetic structures are combined with other structures, their auxetic mechanism is often reduced. In order to reduce the loss of auxetic mechanism and increase stiffness, Baran et al.²¹ obliquely embedded the rod into the traditional re-entrant structure. The mechanical properties of the re-entrant structure were studied by changing the geometric and material parameters. Chen et al.²² proposed a lightweight auxetic structure by embedding the support rod into the rotating square structure. The combination of the auxetic structures with other structures affects the energy absorption capability.^{23,24} It was found that the combination of the re-entrant structure and hexagonal structure has better energy absorption capability than that of the hexagonal structure.²⁵ To improve the energy absorption capability, three kinds of the auxetic structures were compared by embedding different ribs into the classic re-entrant structures.²⁶

To achieve better integrity, sufficient constraints are often imposed between the embedded structure and auxetic structure for the composite auxetic structure. Adjusting mechanical properties often requires changing the shape of the structure. However, due to the existence of too many constraints, the embedded structure or auxetic structure cannot be deformed independently. When one structure is changed to adjust mechanical properties, other structures are often changed as well. In this paper, the independent deformation of the embedded structure and re-entrant structure was achieved in the proposed composite auxetic structure with flexible deformation (CASwFD). The effects of the embedded structure and re-entrant structure on the mechanical properties of the proposed composite auxetic structure were studied by the using rate of change of mechanical properties. This study found that the auxetic mechanism of the proposed auxetic structure was improved due to the reduction of the constraints between the embedded structure and re-entrant structure.

2 | THE PROPOSED COMPOSITE AUXETIC STRUCTURE

As shown in Figure 1(A), there are four fixed constraints ($u_x = u_y = u_z = 0$ and $rot_x = rot_y = rot_z = 0$) between the embedded structure and re-entrant structure of the rhombic grid embedded enhanced honeycomb (RGEEH).¹⁷ When the shape of the re-entrant structure changes, it drives the embedded structure to deform (comparing the light and dark structure). Similarly, when the shape of the embedded structure changes, the re-entrant structure also changes. This makes the adjustment of mechanical properties complicated. To solve the above question, the top and bottom fixed constraints of the RGEEH were removed. And a CASwFD was proposed in Figure 1(B). It can be seen from Figure 1(C)–(E) that the embedded structure and re-entrant structure can deform independently. In this way, the effects of the embedded structure and re-entrant structure on the mechanical properties of the overall structure can be separated.

3 | THEORETICAL ANALYSIS

3.1 | Simplification

The CASwFD under uniaxial compression loading was displayed on Figure 2(A). The lengths of the horizontal and slant rods of the re-entrant structure are h_0 and l_0 , respectively. And their thicknesses are t_0 . The length and thickness of the slant rod of the embedded structure are l_1 and t_1 , respectively. The angles θ_0 and θ_1 are formed by slant rods of the re-entrant structure and embedded structure with X direction, respectively.

Based on the geometrical and loading symmetry of the CASwFD, the rods AB, BC, and CD were adopted as the representative structure to analyze the mechanical properties of the CASwFD. As shown in Figure 2(B), because the points

FIGURE 1 (A) The rhombic grid embedded enhanced honeycomb¹⁸; (B) The composite auxetic structure with flexible deformation (CASwFD); (C) CASwFD-1: the embedded structure (the red structure) is changed and the re-entrant structure remains unchanged (the blue structure); (D) CASwFD-2: The re-entrant structure is changed (the length of the horizontal rod is changed, and the length of the slant rod remains the same) and the embedded structure remains unchanged; (E) CASwFD-3: The re-entrant structure is changed (the length of the horizontal rod remains unchanged, the length of the slant rod is changed) and the embedded structure remains unchanged

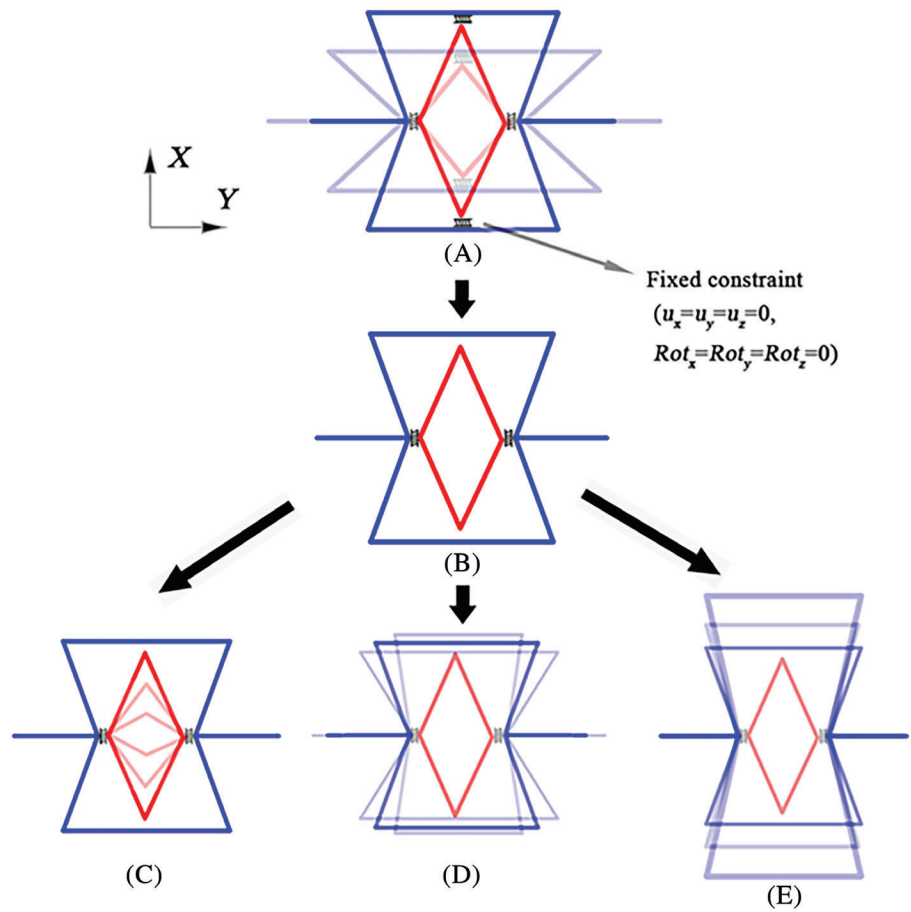
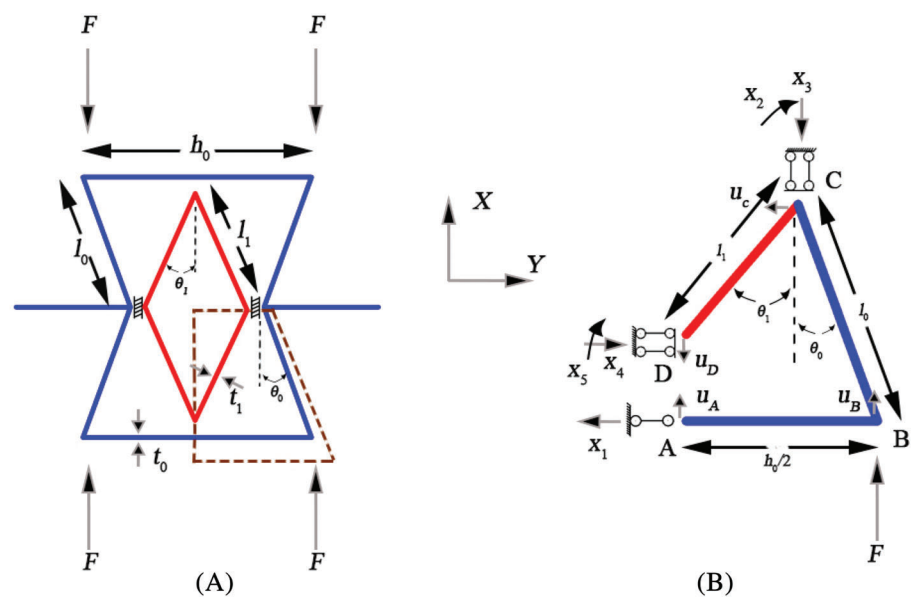


FIGURE 2 (A) Geometric parameters of the CASwFD; (B) the representative structure



A and D are on the left-right symmetry plane of the CASwFD, under the compression of the vertical force F , they only cause vertical displacement u_A and u_D . And the point C is on the upper and lower symmetry plane of the CASwFD, which only causes horizontal displacement u_C . In the deformation process of the rod AB, the displacement of point A is equal to that of the point B ($u_A = u_B$). Thus, the rod AB is only subjected to axial force x_1 . Due to the deformations of the rods BC and CD dominated by bending, the point C is subjected to bending moment x_2 and vertical reaction force x_3 . And the point D is subjected to bending moment x_5 and horizontal reaction force x_4 .

3.2 | Model analysis

The force method and Mohr's theorem were applied to analyze this problem. The unknown reaction force x_1 and bending moment x_2 were employed to set up canonical equation of force method:

$$\delta_{11}x_1 + \delta_{12}x_2 + V_{1p} = 0, \quad (1)$$

$$\delta_{21}x_1 + \delta_{22}x_2 + V_{2p} = 0. \quad (2)$$

The δ_{ij} is the displacement along the x_i direction caused by the unit force $x_j = 1$. V_{ip} is the displacement along x_i direction generated by the force F . Because the deformations of the rods BC and CD are mainly dominated by bending, their shear and axial deformations can be ignored. Therefore, δ_{11} , δ_{22} , δ_{12} , δ_{21} , V_{1p} and V_{2p} in Equations (1) and (2) can be expressed as

$$\delta_{11} = \sum \int \frac{\bar{M}_1^2}{EI} ds + \frac{\bar{F}_{N1}^2 l}{EA} = \frac{l_0^3 \cos^2 \theta_0}{3EI_0} + \frac{l_1 l_0^2 \cos^2 \theta_0 - l_1^2 l_0 \cos^2 \theta_1 \cos^2 \theta_0 + (1/3)l_1^3 \cos^2 \theta_1}{EI_1} + \frac{h_0}{2EA_0} \quad (3)$$

$$\delta_{22} = \sum \int \frac{\bar{M}_2^2}{EI} ds = \frac{l_1}{EI_1}, \quad (4)$$

$$\delta_{12} = \delta_{21} = \sum \int \frac{\bar{M}_1 \bar{M}_2}{EI} ds = \frac{l_1 l_0 \cos \theta_0 - (1/2)l_1^2 \cos \theta_1}{EI_1}, \quad (5)$$

$$V_{1p} = \sum \int \frac{\bar{M}_1 M_p}{EI} ds = \frac{-(1/3)Fl_0^3 \cos \theta_0 \sin \theta_0}{EI_0} - \frac{Fl_1 l_0^2 \cos \theta_0 \sin \theta_0 - (1/2)Fl_1^2 l_0 \sin \theta_0 \cos \theta_1}{EI_1} \quad (6)$$

and

$$V_{2p} = \sum \int \frac{\bar{M}_2 M_p}{EI} ds = \frac{-Fl_1 l_0 \sin \theta_0}{EI_1}, \quad (7)$$

respectively. \bar{M}_i is the bending moment generated by unit force $x_i = 1$ at any section of the basic structure. M_p is the bending moment generated by the force F in the basic structure. E is the Young's modulus of the material. $I_i = (bt_i^3)/12$ is second moment of area where b is the thickness of structure in out-plane direction. And $A_0 = bt_0$ is the cross-section area of the rods AB and BC. By substituting Equations (3)–(7) into Equations (1) and (2), x_1 and x_2 are obtained as

$$x_1 = \frac{(Fl_0^3 \cos \theta_0 \sin \theta_0)/(3EI_0)}{(l_0^3 \cos^2 \theta_0)/(3EI_0) + (l_1^3 \cos^2 \theta_1)/(12EI_1) + h_0/(2EA_0)}, \quad (8)$$

and

$$x_2 = Fl_0 \sin \theta_0 - \frac{(1/EI_0)(1/3)Fl_0^3 \cos \theta_0 \sin \theta_0 [l_0 l_1 \cos \theta_0 - (1/2)l_1^2 \cos \theta_1]}{(l_1 l_0^2 \cos^2 \theta_0)/(3EI_0) + (l_1^4 \cos^2 \theta_1)/(12EI_1) + (l_1 h_0)/(2EA_0)}, \quad (9)$$

respectively. According to the superposition principle, the distribution of moment M of the representative structure in Figure 2(B) can be obtained as

$$M = \bar{M}_1 x_1 + \bar{M}_2 x_2 + M_p. \quad (10)$$

Based on Mohr's theorem, the unit virtual force x_6 and horizontal force x_7 were applied to points C and B. Therefore, the displacements of the point C in Y direction and the point B in X direction are

$$u_c = \sum \int \frac{\bar{M}_6 M}{EI} ds = \frac{3Fl_1^2 l_0 \sin \theta_0 - 3x_1 l_1^2 l_0 \cos \theta_0 + 2x_1 l_1^3 \cos \theta_1 - 3x_2 l_1^2}{6EI_1} \quad (11)$$

and

$$u_B = \sum \int \frac{\bar{M}_7 M}{EI} ds = \frac{[l_0^2 \sin \theta_0 (Fl_0 \sin \theta_0 - x_1 l_0 \cos \theta_0)]}{3EI_0} + \frac{[l_1 l_0 \sin \theta_0 (Fl_0 \sin \theta_0 - x_1 l_0 \cos \theta_0 + (x_1 l_1 \cos \theta_1)/2 - x_2)]}{EI_1}, \quad (12)$$

respectively. The strains of the representative structure in Y and X directions are

$$\epsilon_y = \frac{u_c}{(h_0/2) + l_1 \sin \theta_1} \quad (13)$$

and

$$\epsilon_x = \frac{u_B}{l_0 \cos \theta_0}. \quad (14)$$

respectively. The stress caused by the force F on the representative structure is

$$\sigma = \frac{2F}{bh_0}. \quad (15)$$

The Poisson's ratio and Young's modulus of the CASwFD can be obtained as

$$\mu = -\frac{\epsilon_y}{\epsilon_x} \quad (16)$$

and

$$E_0 = \sigma \epsilon_x, \quad (17)$$

respectively.

4 | FINITE ELEMENT MODEL

Figure 3 shows the finite element model and boundary conditions of the CASwFD for elastic analysis. The CASwFD was modeled using SOLID186 which is a higher order 3D 20-node solid element that exhibits quadratic displacement behavior. The calculation of the Poisson's ratio and Young's modulus of the CASwFD did not consider large deformation. The parameters of matrix material were used as: the Young's modulus $E = 69$ GPa, Poisson's ratio $\mu_0 = 0.33$, yield strength $\sigma_{ys} = 76$ Mpa and density $\rho_s = 2700$ kg/m³. The mesh size (0.08 mm) made the average mesh quality reach 0.99, which is enough to prove the accuracy of the results. The compressive force $F = 0.1$ N was applied to the two end points of the top surface of the CASwFD. The application position of the force F was the same as that of the theoretical analysis. Fixed constraint was imposed on the bottom of the CASwFD. The degree of freedom in the Z direction of the CASwFD was restricted. Under the compressive force F , distance V between points F_1 and F_2 in the X direction, and distance H between points E_1 and E_2 in the Y direction were used to calculate Poisson's ratio and relative Young's modulus.

Dynamic simulation was used to study energy absorption capability. Figure 4 shows the finite element model and boundary conditions of the CASwFD for dynamic analysis. As shown in the Figure 4, 8*8 cell model was established. The impact velocity $v(5$ m/s) along the X direction was applied to the upper rigid plate, and the bottom of the model was fixed. In order to prevent out-of-plane expansion, the displacement of the model in the Z direction was constrained. In the compression process, single-surface contact was used between the model walls, and surface-to-surface contact between the model and the rigid plate was used. The effect of friction between the model walls was not considered. The Shell 163

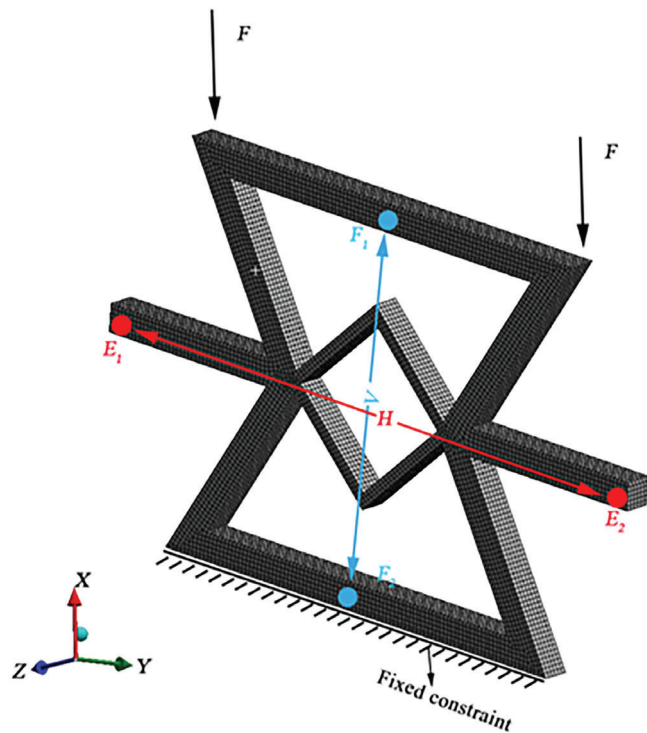


FIGURE 3 Finite element model of the CASwFD for elastic analysis

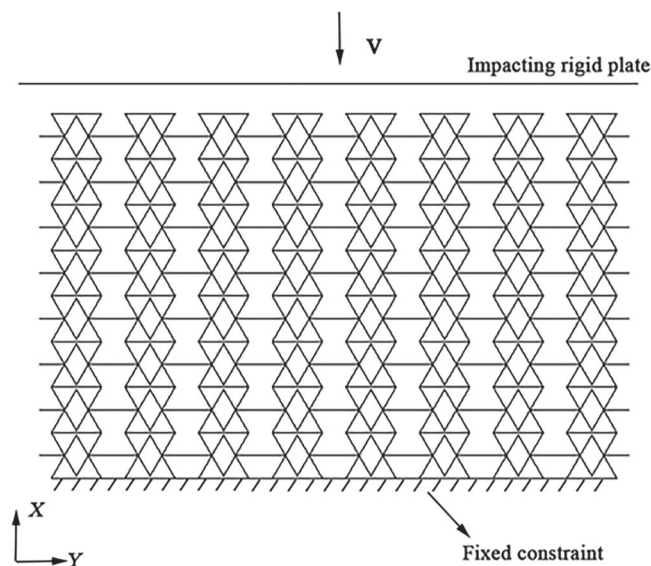


FIGURE 4 Finite element model of the CASwFD for dynamic analysis

unit for dynamic analysis was applied to the model.²⁷ The parameters of material were the same as those of the elastic analysis, and the model was assumed to be ideal elastoplastic.

In order to verify the accuracy of the dynamic analysis, the same numerical model as Reference 27 was built for comparison. Figure 5 shows deformation of the re-entrant structure at impact velocity $v = 7$ m/s. It can be seen from Figure 5 that the deformation of the model established in this paper was basically the same as that of the model in Ref.²⁷

5 | RESULTS AND DISCUSSION

5.1 | Changing the embedded structure

In this section, the mechanical properties of the CASwFD-1 were studied. The change of the embedded structure was defined by the change of angle θ_1 . The geometric parameters of the unchanging re-entrant structure with $h_0 = 9.5$ mm,

FIGURE 5 Comparison of the deformation of the re-entrant structure at impact velocity $v = 7$ m/s. (A) In this paper; (B) In Reference 28

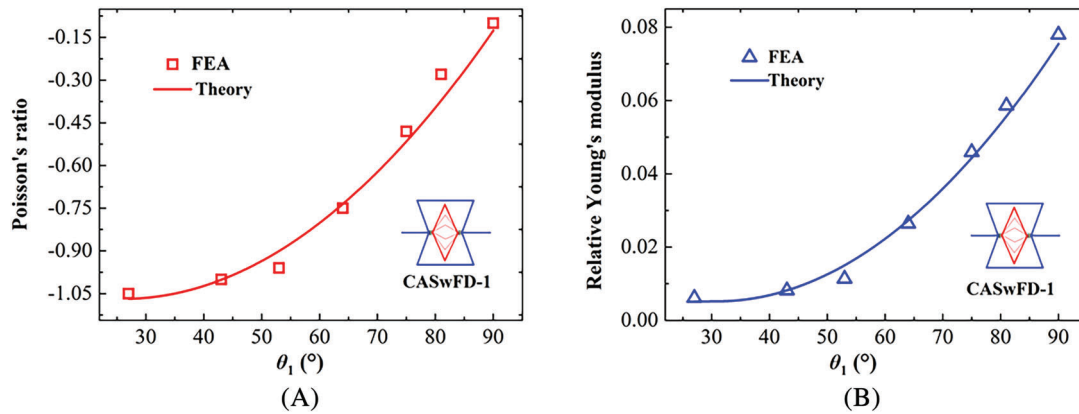
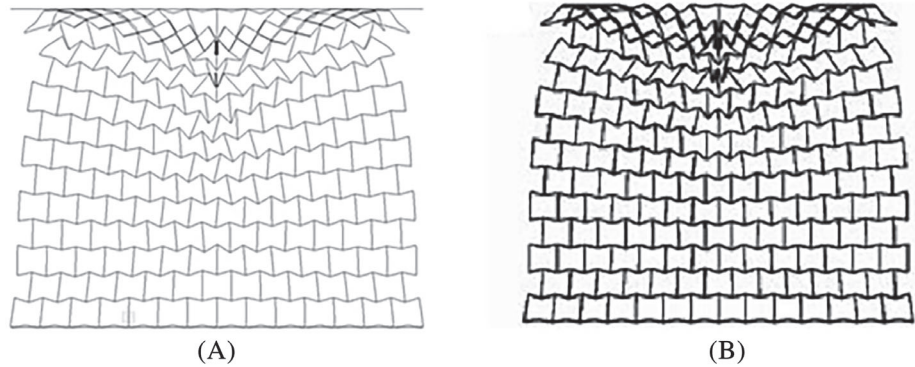


FIGURE 6 Effects of the angle θ_1 on the mechanical properties of the CASwFD-1: (A) Poisson's ratio and (B) relative Young's modulus

$l_0 = 5$ mm, $t_0 = 0.5$ mm, and $\theta_0 = 30^\circ$ were determined. And the thickness t_1 of the embedded structure is 0.2 mm. Figure 6 shows the effects of the angle θ_1 on the Poisson's ratio and relative Young's modulus (E_0/E) of the CASwFD-1. From Figure 6, the finite element results are in good agreement with the theoretical analysis. As shown in Figure 6(A), as the angle θ_1 increased, the Poisson's ratio of the CASwFD-1 increased monotonously. It was obtained that the increase of angle θ_1 leads to the decrease of auxetic mechanism. From Figure 6(B), as the angle θ_1 increased, the relative Young's modulus of the CASwFD-1 increased monotonously. This is because as the angle θ_1 increases, the Young's modulus of the embedded structure in the Y direction can increase, resulting in the higher stiffness and worse auxetic mechanism of the CASwFD-1.

Specific energy absorption (SEA) as the standard to measure the energy absorption capability was employed.²⁵ It is expressed as.²⁸

$$SEA = \frac{EA}{m} = \frac{\int_0^L F(x)dx}{m} \quad (18)$$

where L is the length from the initial point to the beginning of the densification. F is the force corresponding to the length L . m is the mass of the structure. The force–displacement and SEA curves of the CASwFD-1 with various the angle θ_1 were shown in Figure 7. The deformation figures inserted in Figure 7(A) show the deformation of the CASwFD-1 with angle $\theta_1 = 30^\circ$, 53° , and 81° in the platform stage. It can be seen from the deformation figures that the three structures all presented a V-shaped deformation band at the bottom end,²⁹ but the deformations of their upper parts were different. The force–displacement curves of the three structures were not much different, because the change of the embedded structure has little effect on the CASwFD-1. As shown in Figure 7(B), when the angle θ_1 was between about 27° to 43° and 75° to 90° , the SEA of the CASwFD-1 showed a decreasing trend. When the angle θ_1 was between 43° and 75° , the SEA of the CASwFD-1 showed an increasing trend.

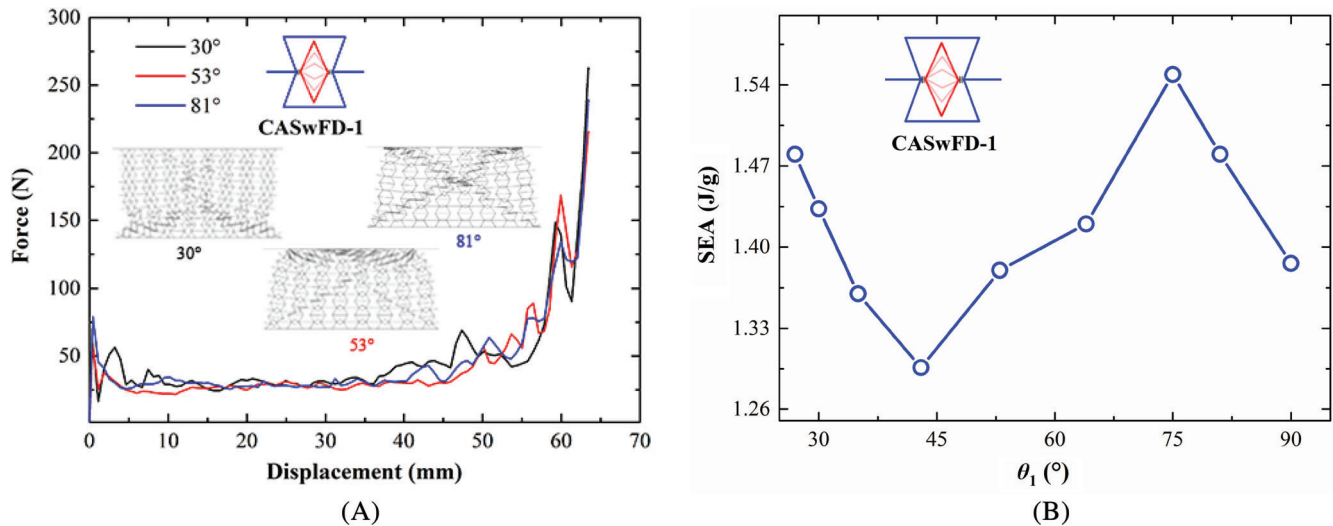


FIGURE 7 (A) The force–displacement and (B) SEA curves of the CASwFD-1 with various the angle θ_1

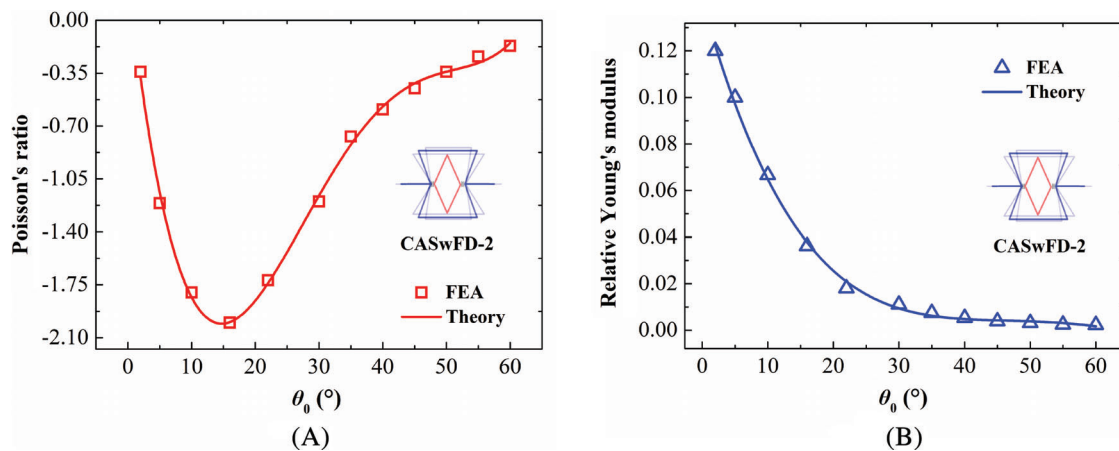


FIGURE 8 Effects of the angle θ_0 on the mechanical properties of the CASwFD-2: (A) Poisson's ratio and (B) relative Young's modulus

5.2 | Changing re-entrant structure

The mechanical properties of the CASwFD-2 and CASwFD-3 were studied. The change of the re-entrant structure was defined by the change of angle θ_0 . The geometric parameters of the unchanging embedded structure with $l_1 = 3.18$ mm, $\theta_1 = 45^\circ$, $t_1 = 0.2$ mm were determined.

Figure 8 shows the effects of angle θ_0 on the Poisson's ratio and relative Young's modulus (E_0/E) of the CASwFD-2 ($l_0 = 5$ mm). From Figure 8, the finite element results are in good agreement with the theoretical analysis. As shown in Figure 8(A), as the angle θ_0 increased, the Poisson's ratio of the CASwFD-2 decreased first and then increased. When the angle θ_0 was about 15° , the Poisson's ratio of the CASwFD-2 reached the minimum value -2 , in which the auxetic mechanism is the best. In Figure 8(B), as the angle θ_0 increased, the relative Young's modulus of the CASwFD-2 decreased monotonously. For energy absorption capability of the CASwFD-2, the force–displacement and SEA curves of the structure with various the angle θ_0 were shown in Figure 9. Similar to the CASwFD-1, the deformation of the CASwFD-2 with angle $\theta_0 = 30^\circ$, 40° , and 55° in the platform stage was shown in Figure 9(A). It can be seen from Figure 9(A) that during the deformation of the platform, the bottoms of the CASwFD-2 with angle $\theta_0 = 30^\circ$ and 40° also showed V-shaped deformation band, while its upper part showed dense collapse. But dense collapse occurred in the lower part of the CASwFD-2 with $\theta_0 = 55^\circ$. In Figure 9(A), as the angle θ_0 of the CASwFD-2 increased, its platform stage became shorter, but the

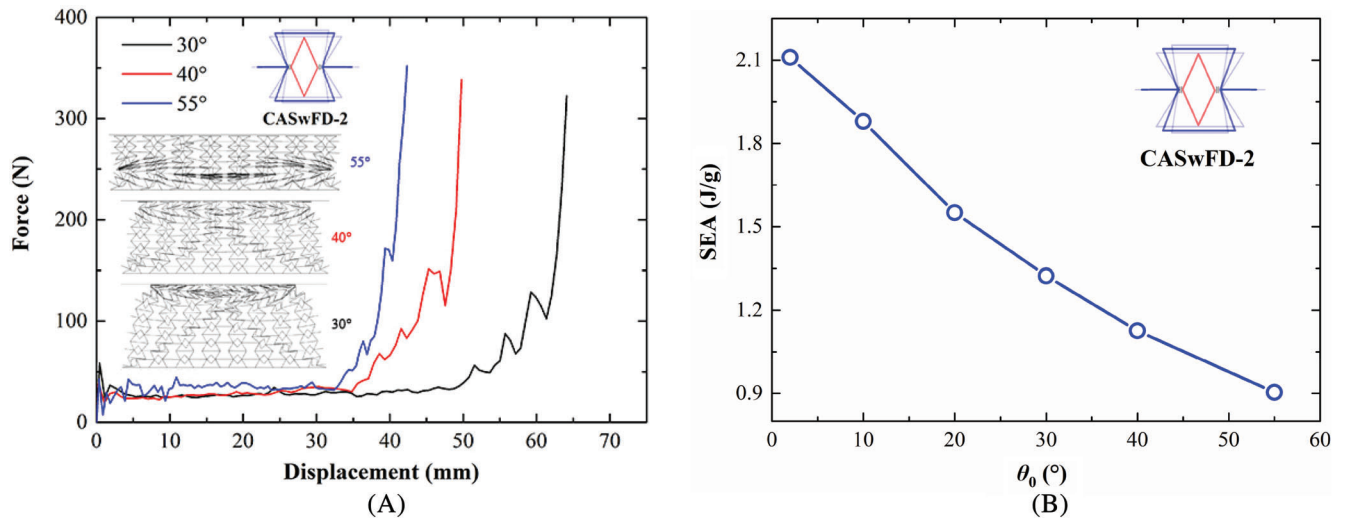


FIGURE 9 (A) The force–displacement and (B) SEA curves of the CASwFD-2 with various the angle θ_0

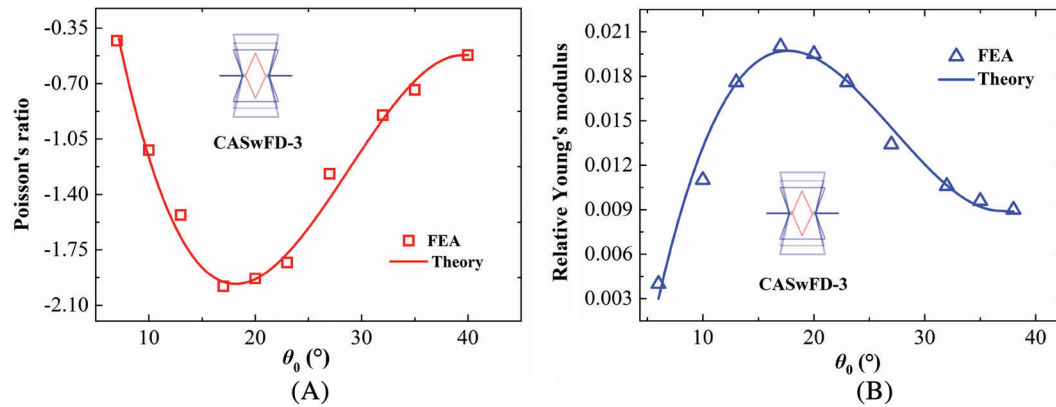


FIGURE 10 Effects of the angle θ_0 on the mechanical properties of the CASwFD-3: (A) Poisson's ratio and (B) relative Young's modulus

value of the platform force was not much different. The platform stage has an important effect on the energy absorption of the auxetic structures.²⁷ As shown in Figure 9(B), as the angle θ_0 increased, the SEA of the CASwFD-2 decreased monotonically.

Figure 10 shows the effects of the angle θ_0 on the Poisson's ratio and relative Young's modulus (E_0/E) of the CASwFD-3 ($h_0 = 9.5$ mm). From Figure 10, the finite element results are in good agreement with the theoretical analysis. As shown in Figure 10(A), as the angle θ_0 increased, the Poisson's ratio of the CASwFD-3 decreased first and then increased. When the angle θ_0 was about 18°, the Poisson's ratio of the CASwFD-3 reached the minimum value -1.98 . In contrast, from Figure 10(B), with increase of the angle θ_0 , the relative Young's modulus of the CASwFD-3 increased first and then decreased, which reached a maximum value 0.02 at angle $\theta_0 = 18^\circ$. For energy absorption capability of the CASwFD-3, the force–displacement and SEA curves of the structure with various the angle θ_0 were shown in Figure 11. As shown in Figure 11(A), the deformation of the CASwFD-3 with angle $\theta_0 = 23^\circ$, 30° , and 40° at the platform stage was similar to that of the CASwFD-2 with angle $\theta_0 = 30^\circ$, 40° , and 55° , respectively. And as the angle θ_0 increased, the platform stage of the CASwFD-3 also became shorter. In Figure 11(B), similar to Figure 10(B), as the angle θ_0 increased, the SEA of the CASwFD-3 monotonically decreased.

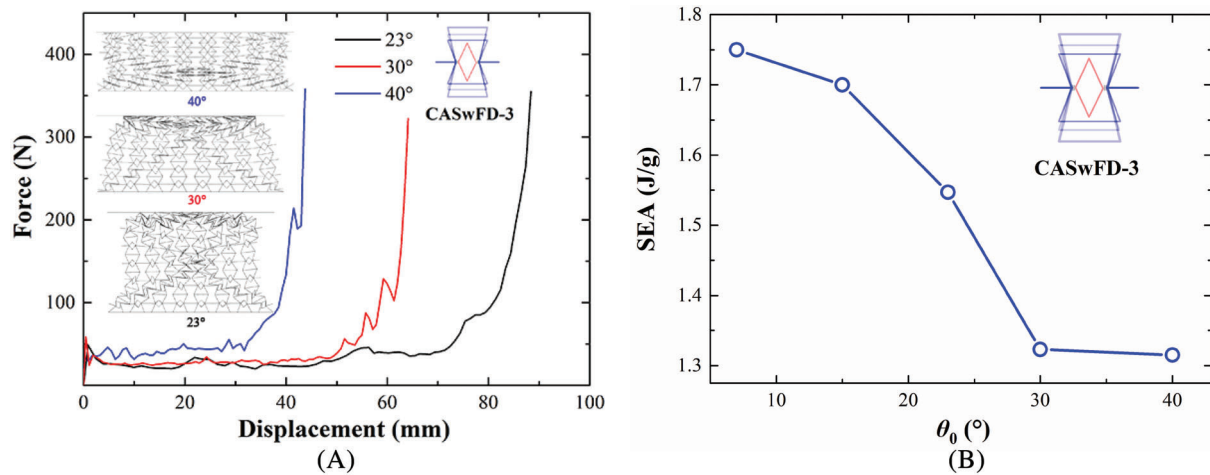


FIGURE 11 (A) The force–displacement and (B) SEA curves of the CASwFD-3 with various the angle θ_0

Structure	$\Delta\mu$	$\Delta m(\text{g})$	$\Delta(E_0/E)$	$\Delta m(\text{g})$	$\Delta EA(\text{J})$	$\Delta m(\text{g})$
CASwFD-1	0.95	0.00124	0.072	0.00124	0.184	0.448
					0.253	0.363
					0.163	0.284
CASwFD-2	1.66	0.0056	0.118	0.0164	0.957	0.855
	1.83	0.0108				
CASwFD-3	1.55	0.0437	0.016	0.0437	6.926	3.522
	1.46	0.0125	0.011	0.0125		

TABLE 1 $\Delta\mu$, $\Delta(E_0/E)$, ΔEA , and corresponding Δm of CASwFD-1, 2, and 3

5.3 | Comparison of the embedded and re-entrant structures

In order to compare the effects of embedded and re-entrant structures on the CASwFD, the change rate of mechanical properties was calculated using following Equations (19)–(21):

$$C_\mu = \frac{\Delta\mu}{\Delta m}, \quad (19)$$

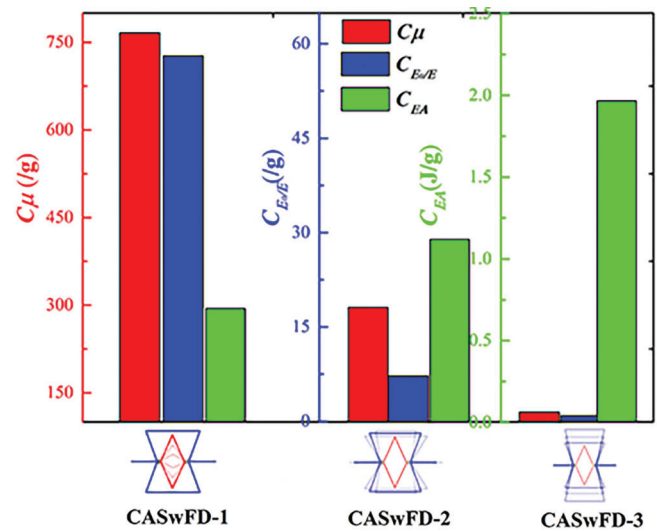
$$C_{E_0/E} = \frac{\Delta\left(\frac{E_0}{E}\right)}{\Delta m}, \quad (20)$$

and

$$C_{EA} = \frac{\Delta EA}{\Delta m}. \quad (21)$$

C_μ , $C_{E_0/E}$, and C_{EA} , respectively, represent the change value in Poisson's ratio, the relative Young's modulus, and energy absorption caused by changing unit mass, respectively. $\Delta\mu$, $\Delta\left(\frac{E_0}{E}\right)$, and ΔEA are the variation values of Poisson's ratio, relative Young's modulus and energy absorption of the embedded or re-entrant structures in the variable range, respectively. Δm is the corresponding mass change. Table 1 shows the data calculated from Figures 6–11. In Table 1, the energy absorption of the CASwFD-1 was divided into three parts. The Poisson's ratio of the CASwFD-2, Poisson's ratio and relative Young's modulus of the CASwFD-3 were divided into two parts in Table 1. Only the maximum values of them were obtained.

FIGURE 12 Comparison of the rate of change of mechanical properties (C_μ , $C_{E_0/E}$, and C_{EA}) between the CASwFD-1, 2, and 3



According to the data in Table 1, Figure 12 shows the values of C_μ , $C_{E_0/E}$ and C_{EA} of the CASwFD-1, 2, 3. As shown in Figure 12, for the C_μ and $C_{E_0/E}$, the values of the CASwFD-1 were the largest, which means that changing every unit mass of the CASwFD-1 can cause the largest variation range of Poisson's ratio and relative Young's modulus. For the C_{EA} , the value of the CASwFD-3 was the largest, which means that changing every unit mass of the CASwFD-3 can cause the largest variation range of energy absorption. Therefore, this also means that the material utilization rates of the CASwFD-1 for Poisson's ratio and relative Young's modulus and the CASwFD-3 for energy absorption reach maximum. The C_μ of the CASwFD-1, the $C_{E_0/E}$, and C_{EA} of the CASwFD-3 were the smallest. However, in Table 1, $\Delta\mu$ and $\Delta(E_0/E)$ of the CASwFD-2 were the largest, indicating that the CASwFD-2 has the largest adjustable range for Poisson's ratio and relative Young's modulus. The CASwFD-1 had the smallest adjustable range for Poisson's ratio. The CASwFD-3 had the smallest adjustable range for relative Young's modulus and energy absorption. The ΔEA of the CASwFD-3 was the largest, indicating that the CASwFD-3 has the largest adjustable range for energy absorption. The CASwFD-1 had the smallest adjustable range for Poisson's ratio and energy absorption. And the CASwFD-2 had the smallest adjustable range for relative Young's modulus.

5.4 | Comparison of auxetic mechanism

The auxetic mechanisms of the CASwFD were compared with the reported RGEH.¹⁷ Because of the unchanged re-entrant structure in the CASwFD-1, there is only one the RGEH corresponding to the CASwFD-1. By calculation, the Poisson's ratio μ of the RGEH is 0.13. Compared to Figure 6(A), Poisson's ratio μ of the RGEH is larger. The comparisons of the Poisson's ratio of the CASwFD-2 and CASwFD-3 with the RGEH at different angles θ_0 were shown in Figure 13. As shown in Figure 13(A), with increase of the angle θ_0 , the Poisson's ratio of the RGEH was positive, while that of the CASwFD-2 was negative. From Figure 13(B), the Poisson's ratio of the CASwFD-3 was larger than that of the RGEH when the angle θ_0 was less than 12° . These results show that the CASwFD has better auxetic mechanism than RGEH. Based on Maxwell's stability criterion,^{30,31} as shown in the following Equation (22)

$$M = n - 2j + 3, \quad (22)$$

the Maxwell's stability factor M of the RGEH is 0. Thus, the RGEH is the deformation dominated by stretching. When the top and bottom constraints between the embedded and the re-entrant structures of the RGEH are removed to obtain the CASwFD, the Maxwell's stability factor M of the CASwFD is less than 0. The deformation of the structure is transformed into bending-dominant deformation, which enhances the shrinkage of the structure in the Y direction. This means that the auxetic mechanism of the structure is improved.

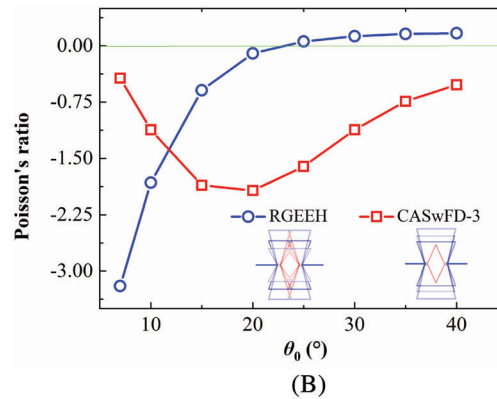
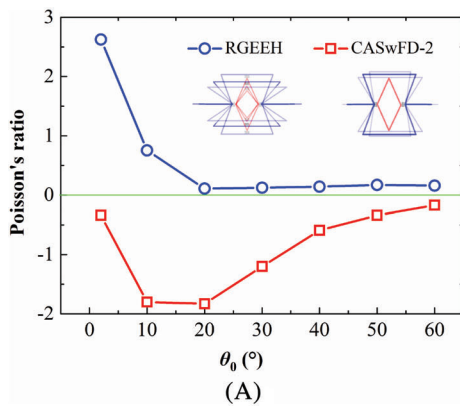


FIGURE 13

Comparison of the Poisson's ratio: (A) RGEEH versus CASwFD-2; (B) RGEEH versus CASwFD-3

6 | CONCLUSION

A CASwFD was proposed, in which the embedded and the re-entrant structures could deform independently to adjust the mechanical properties. By using theoretical and numerical analysis, the effects of changes in embedded and re-entrant structures on the overall structure's Poisson's ratio, relative Young's modulus, and energy absorption were studied. The results showed that as the angle θ_1 (CASwFD-1) of the embedded structure increased, the Poisson's ratio and relative Young's modulus of the structure monotonically increased. The energy absorption first decreased, then increased and finally decreased. When the angle θ_0 (CASwFD-2,3) of the re-entrant structure increased, the Poisson's ratio of the structure first increased and then decreased. The energy absorption decreased monotonically. The relative Young's modulus of the CASwFD-2 decreased monotonically, while the relative Young's modulus of the CASwFD-3 increased first and then decreased. In addition, the rate of change of mechanical properties was studied to compare the effects of embedded and re-entrant structures on the overall structure. It was found that the utilization rate of the material can reach an optimal value by changing the embedded structure for Poisson's ratio and relative Young's modulus and changing the re-entrant structure for energy absorption. By changing the re-entrant structure, the mechanical properties of the overall structure can be adjusted in a wider range. Finally, based on the Maxwell's stability criterion, the auxetic mechanisms of the CASwFD were compared with reported auxetic structure (RGEEH). It was found that the CASwFD dominated by bending has better auxetic mechanism than the RGEEH. It is expected that the proposed structure may provide a new way for the design of the composite auxetic structure.

ACKNOWLEDGMENTS

This work was supported by the Taishan Scholar Project of Shandong Province (No. TSHW20130956) and Natural Science Foundation of Shandong Province, China (No. ZR2017MA013).

CONFLICT OF INTEREST

The authors declare no competing financial interest.

AUTHOR CONTRIBUTIONS

Zengqin Shi: Data curation; formal analysis; writing-original draft. **Qing Wang:** Supervision; writing-review & editing. **Yunfeng Li:** Data curation; formal analysis. **Ning Wang:** Data curation; formal analysis. **Lulu Lei:** Data curation; formal analysis. **Xiaodong Li:** Data curation; formal analysis.

DATA AVAILABILITY STATEMENT

The data that support the findings of this study are available from the corresponding author upon reasonable request.

ORCID

Qing Wang  <https://orcid.org/0000-0001-7228-6472>

REFERENCES

1. Lakes RS. Foam structures with a negative Poisson's ratio. *Science*. 1987;235:1038-1040.
2. Miller W, Smith CW, Evans KE. Honeycomb cores with enhanced buckling strength. *Compos Struct*. 2011;93:1072-1077.

3. Henys P, Vomacko V, Ackermann M, Sobotka J, Solfronk PSJ, Capek L. Normal and shear behaviours of the auxetic metamaterials: homogenisation and experimental approaches. *Meccanica*. 2019;54:831-839.
4. Hu LL, Zhou MZ, Deng H. Dynamic indentation of auxetic and non-auxetic honeycombs under large deformation. *Compos Struct*. 2019;207:323-330.
5. Choi JB, Lakes RS. Fracture toughness of re-entrant foam materials with a negative poisson's ratio: experiment and analysis. *Int J Fatigue*. 1996;80:73-83.
6. Ncemer B, Kramberger J, Vuherer T, Glodez S. Fatigue crack initiation and propagation in re-entrant auxetic cellular structures. *Int J Fatigue*. 2019;126:241-247.
7. Wang H, Lu ZX, Yang ZY, Li X. A novel re-entrant auxetic honeycomb with enhanced in-plane impact resistance. *Compos Struct*. 2019;208:758-770.
8. Lipton JJ, MacCurdy R, Manchester Z, Chin L, Cellucci D, Rus D. Handedness in shearing auxetics creates rigid and compliant structures. *Science*. 2018;360:632-635.
9. Ren X, Das R, Tran P, Ngo TD, Xie YM. Auxetic metamaterials and structures: a review. *Smart Mater Struct*. 2018;27:023001.
10. Larsen UD, Sigmund O, Bouwstra S. Design and fabrication of compliant micromechanisms and structures with negative Poisson's ratio. *J Microelectromech S*. 1997;6:99-106.
11. Grima JN, Jackson R, Alderson A, Evans KE. Do zeolites have negative Poisson's ratios. *Adv Mater*. 2000;12:1912-1918.
12. Jiang YY, Rudra B, Shim J, Li YN. Limiting strain for auxeticity under large compressive deformation: chiral vs. re-entrant cellular solids. *Int J Solids Struct*. 2019;162:87-95.
13. Yu R, Luo W, Yuan H, Liu JX, He WT, Yu ZX. Experimental and numerical research on foam filled re-entrant cellular structure with negative Poisson's ratio. *Thin Wall Struct*. 2020;153:106679.
14. Guo MF, Yang H, Ma L. Design and characterization of 3D AuxHex lattice structures. *Int J Mech Sci*. 2020;181:105700.
15. Wang K, Chang YH, Chen YW, Zhang C, Wang B. Designable dual-material auxetic metamaterials using three-dimensional printing. *MATER DESIGN*. 2015;67:159-164.
16. Fu MH, Chen Y, Hu LL. A novel auxetic honeycomb with enhanced in-plane stiffness and buckling strength. *Compos Struct*. 2017;160:574-585.
17. Fu MH, Chen Y, Hu LL. Bilinear elastic characteristic of enhanced auxetic honeycombs. *Compos Struct*. 2017;175:101-110.
18. Chen Y, Hu LL. Design and modeling of a combined embedded enhanced honeycomb with tunable mechanical properties. *Appl Compos Mater*. 2018;25:1041-1055.
19. Li X, Lu ZX, Yang ZY, Wang QS, Zhang Y. Yield surfaces of periodic honeycombs with tunable Poisson's ratio. *Int J Mech Sci*. 2018;141:290-302.
20. Li X, Wang QS, Yang ZY, Lu ZX. Novel auxetic structures with enhanced mechanical properties. *Extreme Mech Lett*. 2019;27:59-65.
21. Baran T, Ozturk M. In-plane elasticity of a strengthened re-entrant honeycomb cell. *Eur J Mech A-Solid*. 2020;83:104037.
22. Chen Y, He QH. 3D-printed short carbon fibre reinforced perforated structures with negative Poisson's ratios: mechanisms and design. *Compos Struct*. 2020;236:111859.
23. Wu HX, Zhang XC, Liu Y. In-plane crushing behavior of density graded cross-circular honeycombs with zero Poisson's ratio. *Thin Wall Struct*. 2020;151:106767.
24. Li D, Yin JH, Dong L, Lakes RS. Strong re-entrant cellular structures with negative Poisson's ratio. *J Mater Sci*. 2018;53:3493-3499.
25. Xu MC, Xu ZR, Zhang Z, Lei HS, Bai YC, Fang DN. Mechanical properties and energy absorption capability of AuxHex structure under in-plane compression: theoretical and experimental studies. *Int J Mech Sci*. 2019;159:43-57.
26. Chen ZY, Wang Z, Zhou SW, Shao JW, Wu X. Novel negative Poisson's ratio lattice structures with enhanced stiffness and energy absorption capacity. *Materials*. 2018;11:1095.
27. Zhang XC, An LQ, Ding HM, Zhu XY, Rich ME. The influence of cell micro-structure on the in-plane dynamic crushing of honeycombs with negative Poisson's ratio. *J Sandw Struct Mater*. 2015;1:26-55.
28. Zhang W, Yin S, Yu TX, Xu J, et al. Crushing resistance and energy absorption of pomelo peel inspired hierarchical honeycomb. *INT J IMPACT ENG*. 2019;125:163-172.
29. Wei LL, Zhao X, Yu Q, Zhu GH. A novel star auxetic honeycomb with enhanced in-plane crushing strength. *Thin Wall Struct*. 2020;149:106623.
30. Chen ZY, Wu X, Xie YM, Wang Z, Zhou SW. Re-entrant auxetic lattices with enhanced stiffness: a numerical study. *Int J Mech Sci*. 2020;178:105619.
31. Maxwell JC. On the calculation of the equilibrium and stiffness of frames. *Philos Mag*. 1864;27:294-299.

How to cite this article: Shi Z, Wang Q, Li Y, Wang N, Lei L, Li X. Study of mechanical properties and enhancing auxetic mechanism of composite auxetic structures. *Engineering Reports*. 2021;3(12):e12436. <https://doi.org/10.1002/eng2.12436>